Solar Cells Hot Paper

How to cite: *Angew. Chem. Int. Ed.* **2022,** *61,* e202116534
International Edition: doi.org/10.1002/anie.202116534
German Edition: doi.org/10.1002/ange.202116534

Critical Role of Removing Impurities in Nickel Oxide on High-Efficiency and Long-Term Stability of Inverted Perovskite Solar Cells

Shuangjie Wang[+], Yuke Li[+], Jiabao Yang, Tong Wang, Bowen Yang, Qi Cao, Xingyu Pu, Lioz Etgar, Jian Han, Junsong Zhao, Xuanhua Li, and Anders Hagfeldt*

Abstract: The performance enhancement of inverted perovskite solar cells applying nickel oxide (NiO_x) as the hole transport layer (HTL) has been limited by impurity ions (such as nitrate ions). Herein, we have proposed a strategy to obtain high-quality NiO_x nanoparticles via an ionic liquid-assisted synthesis method (NiO_x-IL). Experimental and theoretical results illustrate that the cation of the ionic liquid can inhibit the adsorption of impurity ions on nickel hydroxide through a strong hydrogen bond and low adsorption energy, thereby obtaining NiO_x-IL HTL with high conductivity and strong hole-extraction ability. Importantly, the removal of impurity ions can effectively suppress the redox reaction between the NiO_x film and the perovskite film, thus slowing down the deterioration of device performance. Consequently, the modified inverted device shows a striking efficiency exceeding 22.62 %, and superior stability maintaining 92 % efficiency at a maximum power point tracking under one sun illumination for 1000 h.

[*] Dr. S. Wang,[+] Dr. J. Yang, Dr. T. Wang, Dr. Q. Cao, Dr. X. Pu, Dr. J. Han, Dr. J. Zhao, Prof. X. Li
State key Laboratory of Solidification Processing
Center for Nano Energy Materials
School of Materials Science and Engineering
Northwestern Polytechnical University
710000 Shaanxi Xi'an (China)
E-mail: lixh32@nwpu.edu.cn

Dr. Y. Li[+]
Department Department of Chemistry and Centre for Scientific Modeling and Computation, Chinese University of Hong Kong
999077 Shatin, Hong Kong (P.R. China)

Dr. B. Yang
Department of Chemistry-Ångström Laboratory
Uppsala University
75120 Uppsala (Sweden)

Prof. L. Etgar
Institute of Chemistry, Casali Center for Applied Chemistry, The Hebrew University of Jerusalem
91904 Jerusalem (Israel)

Prof. A. Hagfeldt
Laboratory of Photomolecular Science
Institute of Chemical Sciences and Engineering
School of Basic Sciences
Ecole Polytechnique Fédérale de Lausanne
1015 Lausanne (Switzerland)

[+] These authors contributed equally to this work.

Introduction

The hole transport layer (HTL) has played a dominant role in the device performance and long-term stability of inverted perovskite solar cells (PSCs).[1–6] At present, various organic hole transport materials (HTMs) have been applied, especially poly(3,4-ethylenedioxythiophene): poly(styrenesulfonate) (PEDOT:PSS) and poly(bis(4-phenyl)(2,4,6-trimethylphenyl)amine) (PTAA). However, their complicated fabrication process, intrinsic chemical volatility, poor stability, and high cost hinder the large-scale application toward commercialization. By comparison, several inorganic HTMs such as CuSCN,[7,8] NiO_x,[9–12] CuI,[13,14] VO_x and WO_3 have been used as substitutes for organic HTMs.[15–17] Among those, NiO_x has attracted extensive attention because of its high optical transmittance, appropriate work function and inherent stability.[18–22] Currently, NiO_x HTL can be produced by sputtering, electrodeposition, or pulsed laser deposition technologies.[23–28] However, these methods are stringent and costly. Therefore, as a low-cost alternative, researchers have developed a chemical precipitation method to successfully synthesize NiO_x nanoparticles for the preparation of HTL,[29–31] but the device efficiency and stability of these NiO_x-based PSCs are still lagging behind.

The traditional low-temperature-processed NiO_x nanoparticles can be obtained by a simple and flexible two-step method,[3,21,30,32] in which $Ni(OH)_2$ is firstly prepared through the reaction between $Ni(NO_3)_2$ and NaOH, then it is calcined to obtain NiO_x nanoparticles, as shown in Figure 1a.[9,33–36] However, NO_3^- ions are produced during the synthesis and cannot be completely removed by the subsequent process. Instead, they are embedded in the $Ni(OH)_2$ layer, causing impurities in the NiO_x layer and consequently deteriorating the device efficiency and long-term stability.[32,35] Although these impurity ions could be removed at high temperatures, they will cause poor dispersion of the generated NiO_x in aqueous solutions and seriously affect the subsequent preparation of HTLs by solution spin coating.[32,37,38] Therefore, it is particularly important to effectively inhibit the impurity ions from adsorbing on the surface of NiO_x nanoparticles for realizing high-efficiency PSCs under low-temperature process conditions.

Herein, we propose a simple route to obtain high-quality NiO_x nanoparticles via ionic liquid (IL)-assisted synthesis (NiO_x-IL). As shown in Figure 1a, different from the traditional method, we added 1-butyl-3-methylimidazolium tetrafluoroborate ($[BMIm]BF_4$) IL into the $Ni(NO_3)_2$ precursor

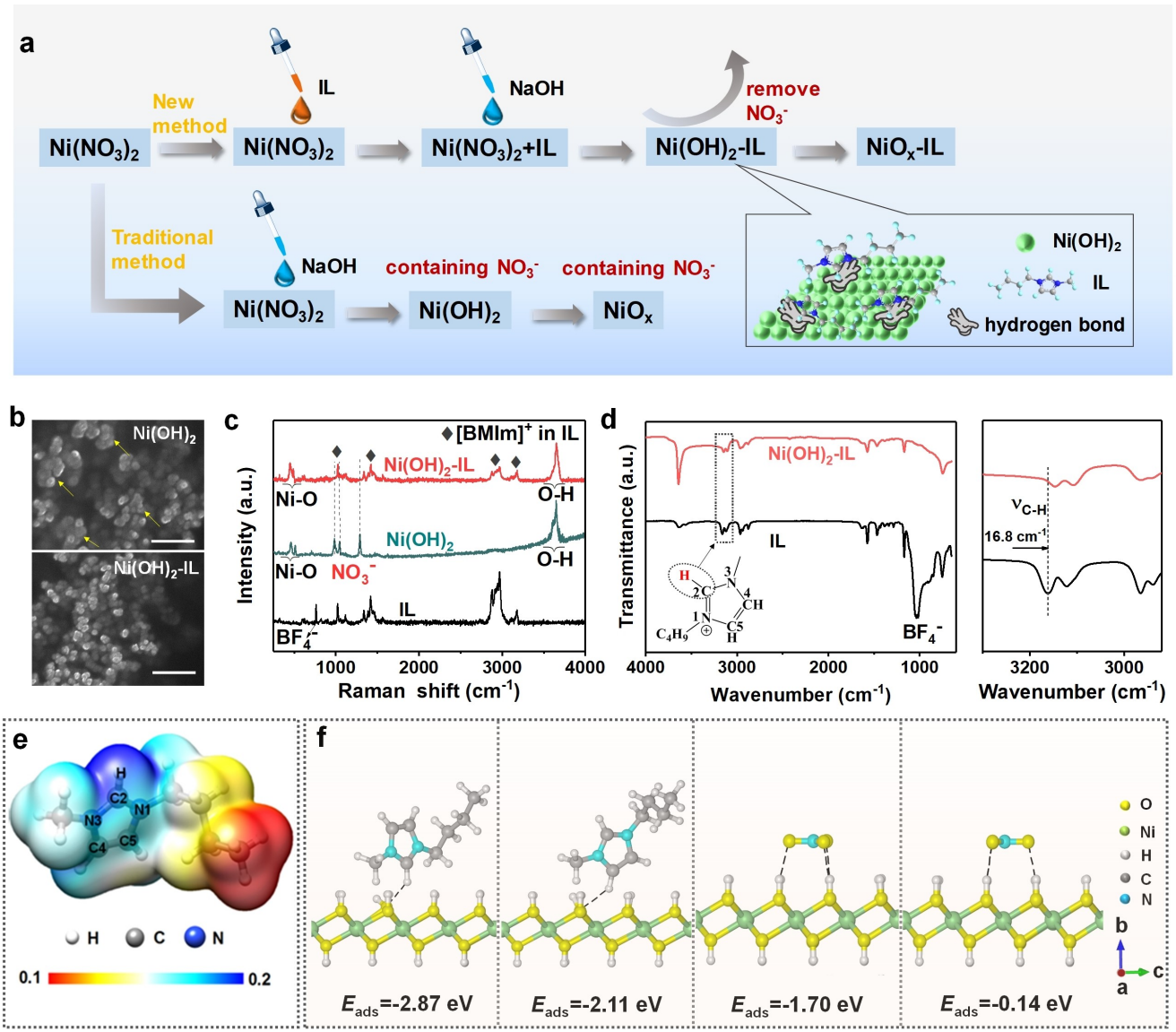

Figure 1. a) Synthesis of NiO_x and NiO_x-IL nanoparticles. b) SEM images of $Ni(OH)_2$ and $Ni(OH)_2$-IL, the scale bar is 500 nm. c) Raman spectra of the pure $[BMIm]BF_4$ IL, control $Ni(OH)_2$, and $Ni(OH)_2$-IL. d) FT-IR spectra of the pristine IL and $Ni(OH)_2$-IL, the right view represents an enlarged image of FT-IR spectra in the range of 2900–3300 cm^{-1}. e) Calculated ESP profiles of the $[BMIm]BF_4$. f) Adsorption configurations of $[BMIm]^+$ and NO_3^- on $Ni(OH)_2$: For $[BMIm]^+$ adsorption, two possible models for the formation of hydrogen bonds on imidazole rings were proposed based on ESP results; For NO_3^- adsorption, the two adsorption configurations refer to that the lower part of N atom in NO_3^- corresponds to O or Ni atom in nickel hydroxide when NO_3^- is adsorbed on nickel hydroxide (as can be seen from the top views of adsorption configurations in Figure S3 in the Supporting Informtion).

before reacting with NaOH. Because on the one hand, the $[BMIm]BF_4$ IL is easy to obtain and has high yield; on the other hand, the multifunctional substitution of the imidazole ring creates more chemical bonding sites. In addition, both experimental and theoretical results illustrate that the $[BMIm]^+$ cation has lower adsorption energy than the NO_3^- impurity ions, and can adsorb on the surface of $Ni(OH)_2$ through strong hydrogen bonds, which effectively inhibit the existence of interlayer NO_3^- ions in $Ni(OH)_2$ (termed as $Ni(OH)_2$-IL). Then, the $Ni(OH)_2$-IL nanoparticles were thermally decomposed to produce NiO_x-IL (Figure 1a). The detailed synthesis method is described in the experimental section in the Supporting Information. This strategy can also improve the conductivity and hole extraction ability of the corresponding HTL. More importantly, the removal of impurity ions can effectively suppress the redox reaction at the buried interface between the NiO_x-IL film and the perovskite film, which is conducive to maintaining the good conductivity of HTL, delaying the decomposition of the perovskite light-absorbing layer, and finally improving the device stability. Consequently, the inverted PSC based on NiO_x-IL HTL exhibits a promising power conversion efficiency (PCE) of 22.62 % and markedly enhanced long-

term storage stability and operational stability compared to those of the traditional NiO_x-based devices.

Results and Discussion

The synthesis process of $[BMIm]BF_4$ IL is presented in Figure S1 in the Supporting Information. The molecular structure of synthesized $[BMIm]BF_4$ was confirmed by ^1H NMR, as described in the Supporting Information. The $[BMIm]BF_4$ IL began to lose weight above 390 °C, which ensured its good stability in the preparation of NiO_x-IL nanoparticles (Figure S2 in Supporting Information). In addition, the conjugated structure of the imidazole ring makes the $[BMIm]^+$ have good conductivity. The scanning electron microscopy (SEM) images show that the $Ni(OH)_2$-IL nanoparticles have a small particle size (Figure 1b). We speculate that the long-chain structure of the $[BMIm]BF_4$ IL cation is similar to that of the surfactant, which hinders the aggregation rate of nanoparticles and promotes the generation of nanoparticles with smaller size.[39]

We gained insights into the process of $[BMIm]BF_4$ IL-assisted synthesis by combining experimental measurements and theoretical calculations. Firstly, Raman spectra were provided to define the chemical groups of the control precursor of $Ni(OH)_2$ and target precursor of $Ni(OH)_2$-IL. In Figure 1c, the lattice vibration modes of Ni–O in the Raman spectra of $Ni(OH)_2$ were observed at 450 and 490 cm^{-1}, and the tensile mode of O–H appeared between 3590 and 3700 cm^{-1}.[40] Notably, the peaks at 994, 1047 and 1280 cm^{-1} are attributed to the stretching vibration peak of NO_3^-.[32] These NO_3^- impurity ions are introduced by the synthesis reaction and embedded in the $Ni(OH)_2$ interlayer structure, which cannot be completely removed in the subsequent washing process.[32] Conversely, the vibration peaks of NO_3^- in the Raman spectrum of $Ni(OH)_2$-IL are not observed, and the characteristic vibration peaks of $[BMIm]^+$ can be clearly observed. The results indicate that $[BMIm]BF_4$ IL plays an important role in synthesizing $Ni(OH)_2$-IL. Notably, no characteristic peaks of BF_4^- are observed in Raman spectra. This is due to the fact that a small amount of BF_4^- could be rapid hydrolyzed into F^- by combining with water molecules; then the F^- ions combined with Na^+ ions in solution to form NaF, which were finally removed in the subsequent washing step.[41]

Fourier Transform Infrared Spectroscopy (FTIR) was conducted to verify the molecular interaction between $[BMIm]BF_4$ IL and $Ni(OH)_2$. The infrared characteristic absorption peaks of $[BMIm]^+$ in $Ni(OH)_2$-IL can be clearly observed in Figure 1d. Peaks at 3163 and 3123 cm^{-1} in the spectrum of pure $[BMIm]BF_4$ IL match the stretching vibration peak of C(2)–H on the imidazolium ring (the inset in Figure 1d), and shift 16.8 cm^{-1} to lower wavenumber in the $Ni(OH)_2$-IL. By analyzing the molecular structure of $[BMIm]BF_4$ IL, we found that the six π electrons on the imidazole ring are distributed on five atoms, and mainly concentrated on N atoms of the imidazole ring. Among them, the relatively low electron cloud density of C(2) atom attributes to its location between the two N atoms, which results in the hydrogen atom attaching to C(2) with the strong ability to accept electrons.[42] As evidence, the electrostatic potential (ESP) of $[BMIm]^+$ was calculated based on density functional theory (DFT) to determine the distribution of its electron density. As presented in Figure 1e, the lowest electron density (positive region) of $[BMIm]^+$ is distributed on the H atom connected to C(2). Accordingly, we conjecture that the red shift of FTIR is due to the existence of C(2)–H···O hydrogen bond between C(2)–H in $[BMIm]^+$ and $Ni(OH)_2$-IL. Theoretical calculations were performed to further investigate why the addition of $[BMIm]^+$ can remove NO_3^- impurity ions in $Ni(OH)_2$-IL. According to the above FTIR results, we constructed the stable structure for theoretical modeling where $[BMIm]^+$ and NO_3^- were adsorbed on the surface of $Ni(OH)_2$ respectively, as shown in Figure 1f and Figure S3 in Supporting Information. The calculated results show that the adsorption energy of $[BMIm]^+$ adsorbed on the $Ni(OH)_2$ surface (two different models, −2.87 and −2.11 eV) is lower than that of NO_3^- adsorption (−1.70 and −0.14 eV), especially when $[BMIm]^+$ was adsorbed by C(2)–H···O hydrogen bond. Combining with FTIR and theoretical calculation, it is concluded that the $[BMIm]^+$ is prone to adsorb on the surface of $Ni(OH)_2$ by stable hydrogen bond. Accordingly, it inhibits the adsorption of the NO_3^- impurity ions and provides an important prerequisite for the subsequent production of NiO_x-IL.

We further investigated the properties of control NiO_x and NiO_x-IL prepared from the above-mentioned $Ni(OH)_2$ and $Ni(OH)_2$-IL, respectively. In Figure 2a, the N–O stretching vibration peak of NO_3^- appears obviously as a single broad peak in control NiO_x, which is consistent with the reported literature.[43,44] Instead, the vibration peak of NO_3^- is not observed in NiO_x-IL, and the peaks of $[BMIm]^+$ can still be observed in Raman spectra of NiO_x-IL due to the good thermal stability of $[BMIm]BF_4$ IL. In X-ray diffraction (XRD) spectra, NiO_x and NiO_x-IL show similar diffraction peaks (Figure 2b). SEM measurements show that the NiO_x-IL film is dense (Figure S4 in Supporting Information), which might be due to the small size of NiO_x-IL nanoparticles.[45] The rough root mean square (RMS) of NiO_x and NiO_x-IL films are 4.76 and 2.10 nm (Figure S5 in Supporting Information), respectively. The contact angle of perovskite precursor solution on NiO_x-IL film (20.3°) is slightly smaller than the control NiO_x film (25.8°) (Figure S6 in Supporting Information). The NiO_x and NiO_x-IL films have high light transmittance (Figure S7 in Supporting Information).

X-ray photoelectron spectroscopy (XPS) analysis was performed to clarify the oxidation state of NiO_x-IL and the results were compared with the control NiO_x film. As shown in Figure 2c, the NiO_x and NiO_x-IL films exhibit three main peaks in the spectra of Ni $2p_{3/2}$. The peak centered at 860.8 eV refers to the shakeup process in the typical NiO_x structure and corresponds to the satellite peak.[34] Meanwhile, the peak at 853.3 eV is assigned to Ni^{2+} in Ni–O octahedral bonding structure,[46,47] and the other peak at 855.2 eV is ascribed to Ni^{3+} due to the existence of Ni^{2+} vacancy.[48,49] It has been reported that the excess Ni^{3+} is the

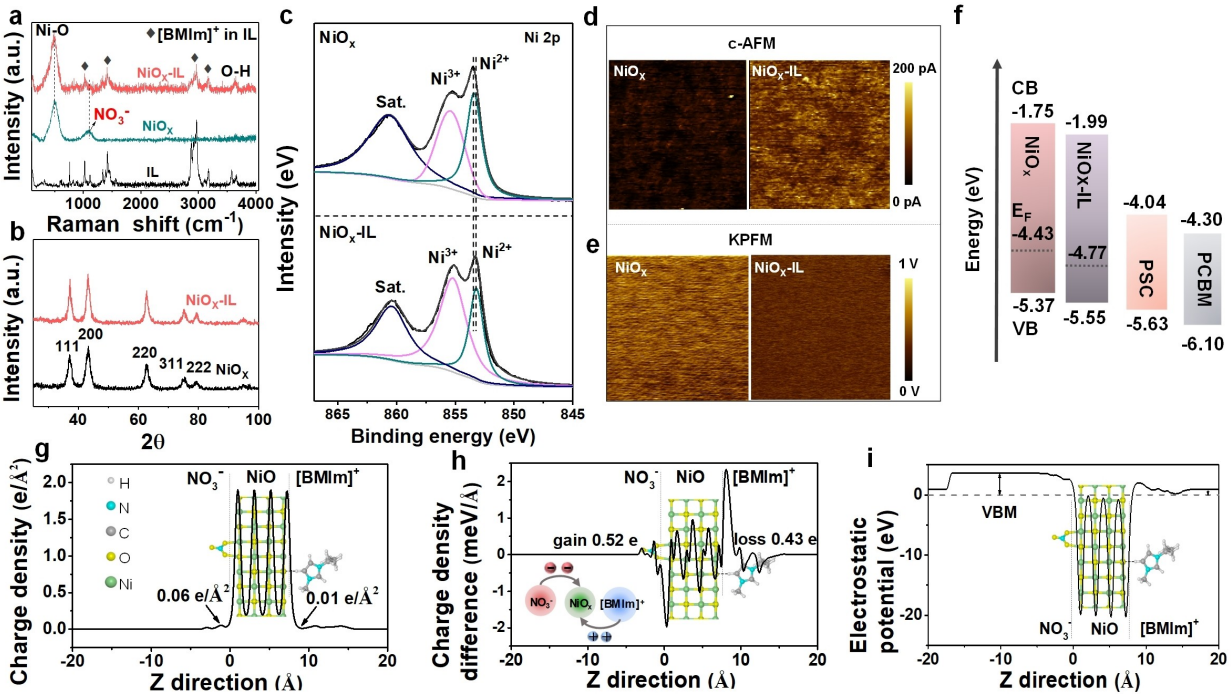

Figure 2. a) Raman spectra and b) XRD spectra of NiO_x and NiO_x-IL. c) XPS spectra of Ni 2p of control NiO_x and NiO_x-IL films. d) c-AFM and e) KPFM images of NiO_x and NiO_x-IL films coated ITO glass. f) Energy band diagram of these different layers based on the parameters calculated from UPS spectra. g) Charge density and h) charge density difference between NiO and IL (or NO_3^-), the inset in Figure 2h illustrates the effect of NO_3^- and $[BMIm]^+$ ions on the gain and loss of electrons in NiO. i) Planar averaged potential of NiO covered by NO_3^- and $[BMIm]^+$, with respect to the energy of VBM.

main reason for the p-type properties of nickel oxide film.[4] Increasing the content of Ni^{3+} can induce the formation of additional holes, reduce the resistivity, and increase the conductivity of nickel oxide.[50–53] As calculated by XPS, the Ni^{3+}/Ni^{2+} ratios of NiO_x-IL film (1.92) is higher than that of the control NiO_x film (1.35), indicating that the hole conductivity of NiO_x-IL film is improved. Moreover, the Ni 2p core level peak of NiO_x-IL layer has an shift of ≈0.18 eV compared to NiO_x layer, which indicates that the change of NiO_x-IL chemical environment compared with NiO_x (as described in the later DFT calculation, electron transfer occurred in the presence of $[BMIm]^+$ adsorption).

We calculated the conductivity of NiO_x and NiO_x-IL films, which is 9.2×10^{-3} and 2.45×10^{-2} mS cm^{-1} (Figure S8 in Supporting Information). The hole mobility increases from 3.7×10^{-3} (NiO_x) to 7.01×10^{-3} (NiO_x-IL) cm^2 V^{-1}·s (Figure S9 in Supporting Information). Furthermore, conductive AFM (c-AFM), as a significant interest to characterize the local charge transport in nanometer scale, has been applied to explore the spatially resolved conductivity of NiO_x and NiO_x-IL film. In Figure 2d, the current flow in the NiO_x-IL film is greater than the control NiO_x film, and the current distribution is uniform, which illustrates the uniform distribution of IL on the NiO_x-IL film. Kelvin probe force microscope (KPFM) was performed to study the influence of IL-assisted synthesis method on the electronic energy level of NiO_x-IL film. The change in work function (W_F) of the measured sample surface is reflected by the contact potential difference (CPD). A lower CPD represents a higher W_F in the local area of the film.[30,54] As illustrated in Figure 2e, the CPD of NiO_x-IL film (0.31 V) is lower than that of the control NiO_x film (0.66 V), and the W_F of NiO_x-IL film (4.79 V) is higher than that of control NiO_x film (4.44 V) (see Supporting Information). Furthermore, the energy band diagram of different films was calculated from ultraviolet photoelectron spectroscopy (UPS, Figures S10 and S11 in Supporting Information). In Figure 2f, compared with control NiO_x film, the valence band (VB) of NiO_x-IL film increases from 5.37 to 5.55 eV, and the Fermi level (E_F) increases from 4.43 to 4.77 eV, which is in accordance with the result of KPFM. The VB offsets for NiO_x and NiO_x-IL relative to perovskites are 0.26 and 0.08 eV, respectively. The decrease of offset is conducive to the rapid hole extraction at the NiO_x-IL/perovskite interface with low energy loss.

The DFT was conducted to further explore the unique effect of NO_3^- and $[BMIm]^+$ on NiO, and the formation mechanism of the increase of Ni^{3+} content after the addition of IL. We placed NO_3^- and $[BMIm]^+$ on each side of NiO (100) surface. The NO_3^- adsorbs on NiO (100) forming O–Ni bond, and the $[BMIm]^+$ adsorbs on NiO (100) through the hydrogen bond (Figure S12 in Supporting Information). As displayed in Figure 2g, the minimum charge density (ρ_{min}) of NiO layer adsorbing NO_3^- impurity ions is 0.06 e Å^{-2}. However, the ρ_{min} of NiO layer adsorbing $[BMIm]^+$ decreases to 0.01 e Å^{-2}. The low charge density indicates that more electron is transferred from NiO to exogenous ions (NO_3^- or $[BMIm]^+$). To confirm the above

conjecture, Figure 2h illustrates the charge density difference with NO_3^- and $[BMIm]^+$ adsorption. There is 0.52 e gain for NiO layer with NO_3^- adsorption; on the contrary, the NiO layer with $[BMIm]^+$ adsorption loses 0.43 e and becomes more positive, thereby increasing the Ni^{3+} concentration. This is consistent with the XPS results. Furthermore, inspired by Tao's work (study on the shift of VB relative to vacuum energy level of nickel oxide adsorbed by halides),[55] we get the VB shift when NiO is covered by NO_3^- and $[BMIm]^+$. As shown in Figure 2i, the adsorption of $[BMIm]^+$ can potentially induce the VB of NiO layer downshift, which contributes to the electron loss of NiO in the presence of $[BMIm]^+$ (inset in Figure 2h). It is consistent with above UPS results. Notably, the shift value of VB from DFT calculation is larger than the shift in the UPS experiment results. We attribute this to the high coverage adsorbates on the NiO surface.

We further evaluated device efficiency based on NiO_x and NiO_x-IL HTL with a configuration of ITO/NiO_x or NiO_x-IL (20 nm)/perovskite (750 nm)/PCBM + C60 (45 nm)/BCP (10 nm)/Cr (5 nm)/Au (100 nm). The composition of the perovskite light-absorbing layer is $Cs_{0.05}(MA_{0.15}FA_{0.85})_{0.95}Pb(I_{0.85}Br_{0.15})_3$. The performance of devices optimized by $[BMIm]BF_4$ IL with different concentrations was provided in Figure S13 and Table S1 in Supporting Information. Figure 3a exhibits the current density-voltage (*J–V*) curves of the optimal PSCs measured under AM 1.5G at 100 mW cm^{-2}, and the detailed photovoltaic parameters are summarized in Table 1. Device using NiO_x-IL HTL delivers an impressive PCE of 22.62 %, with an open circuit voltage (V_{oc}) of 1.13 V, a short circuit current density (J_{sc}) of 23.75 mA cm^{-2}, and a fill factor (FF) of 84.21 %. Conversely, NiO_x-based control device shows a PCE of 19.80 %. On the basis of the band gap of perovskite (1.59 eV), the total V_{oc} loss decreases from 0.50 (NiO_x) to 0.46 V (NiO_x-IL). The distribution of photovoltaic parameters of different devices are shown in Figure S14 in Supporting Information, and its statistical distribution is the same as the change trend of the best photovoltaic parameters. Meanwhile, the device based on NiO_x-IL HTL exhibits

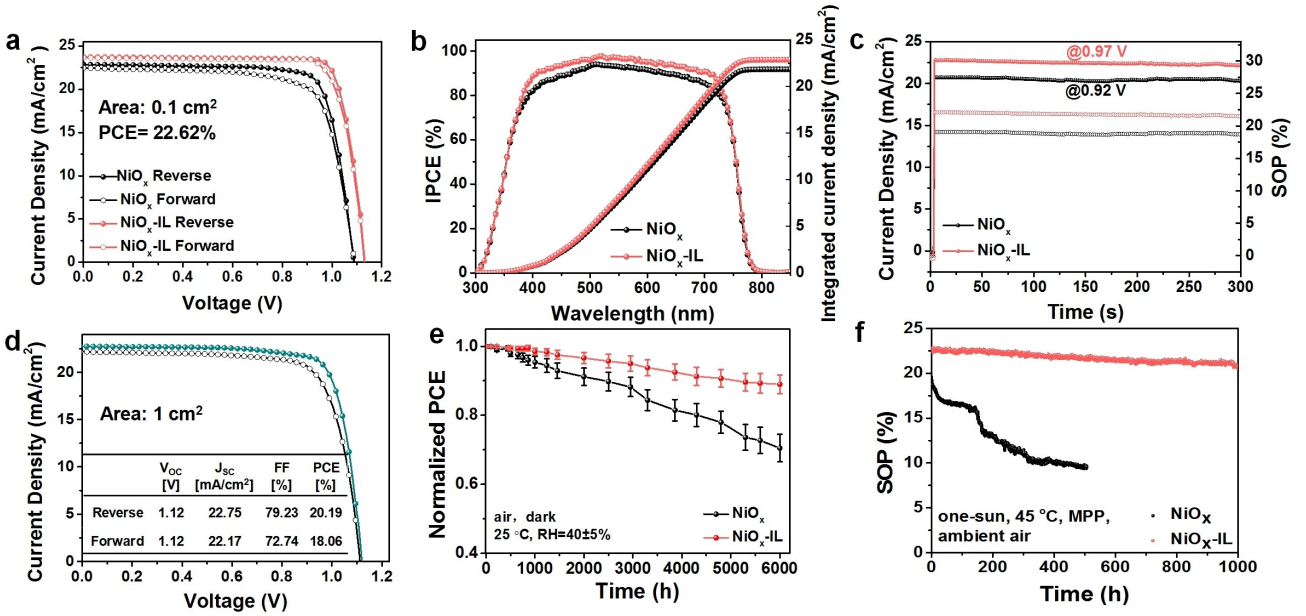

Figure 3. *J–V* characteristics of a) the devices based on NiO_x and NiO_x-IL HTLs under both the reverse and forward scan directions. b) IPCE together with the corresponding integrated current density of these devices. c) Steady-state PCE measured under maximum power point tracking for 300 s of the devices based on NiO_x and NiO_x-IL HTLs. d) *J–V* characteristics of the large area (1 cm^2) device based on NiO_x-IL HTL under both the reverse and forward scan directions. e) PCE of the devices normalized to the initial efficiencies as a function of storage time in dark and ambient air with relative humidity 40 ± 5 %, the data are taken from the average of 10 devices. f) MPP tracking of encapsulated PSCs based on NiO_x and NiO_x-IL HTLs under one-sun irradiation at 45 °C and in ambient air.

Table 1: Statistical photovoltaic parameters of the devices based on NiO_x and NiO_x-IL HTLs under both the reverse and forward scan directions. The scan rate of *J–V* measurement was 0.4 V s^{-1}.

Devices	Scan direction	V_{oc} [V]	J_{sc} [mA cm^{-2}]	FF [%]	PCE [%]	Hysteresis factor	R_s [Ω cm^2]	R_{sh} [Ω cm^2]
NiO_x-IL	Reverse	1.13	23.75	84.21	22.62	0.88	1.20	32 787
	Forward	1.13	23.67	83.82	22.42			
NiO_x	Reverse	1.09	22.85	79.51	19.80	3.53	4.68	8808
	Forward	1.09	22.78	76.73	19.10			

Hysteresis factor $= \frac{PCE_{reverse} - PCE_{forward}}{PCE_{reverse}}$.

negligible hysteresis. The detailed parameters are presented in Table 1. The integrated J_{sc} values from internal photon-to-current efficiency (IPCE) are 21.84 and 22.86 mA cm^{-2} for the device with NiO_x and NiO_x-IL HTLs (Figure 3b), matching well with the results calculated from J–V measurements. A steady-state power output (SPO) of 22.04 % at maximum power point (MPP) were obtain for the PSC based on NiO_x-IL (Figure 3c), indicating the high reliability of the modified device performance. We also tried to prepare large area (1 cm^2) device using blade coating method, and obtained a PCE of 20.19 %, which proves the feasibility of the new strategy for large area devices (Figure 3d). The PCE enhancement of NiO_x-IL-based device is mainly due to the improvement in J_{sc}, V_{oc}, and FF. Since the unchanged optical absorption of devices with NiO_x and NiO_x-IL HTLs (Figure S15 and S16 in Supporting Information), the increment of J_{sc} for NiO_x-IL-based devcie is attributed to the promoted carriers extraction ability;[56,57] the increased V_{oc} likely stems from the reduced interfacial recombination and matched energy level;[58] and the improvement in FF is mainly due to the decreased series resistance (R_s) and increased shunt resistance (R_{sh}), as shown in Figure S17–S20 in Supporting Information and Table 1.

We studied the PCE evolution trend of the devices based on NiO_x and NiO_x-IL HTLs after long-term storage (dark, air, 25 °C, 40 ± 5 % relative humidity). As shown in Figure 3e, the PCE of unencapsulated device using NiO_x-IL HTL remains approximately 90 % after 6000 h storage, while the efficiency of NiO_x-based device decreases to about 71 % of its initial efficiency. More importantly, we conducted operational stability measurements at MPP tracking under one-sun irradiation in ambient air for different encapsulated devices. As depicted in Figure 3f, the NiO_x-based device declined rapidly under MPP tracking, only retained 49 % of its initial SPO after 505 h ageing. In contrast, the NiO_x-IL-based device maintained 92 % of its initial SPO after 1000 h, exhibiting superior operational stability.

Thus, we further investigated the outstanding stability of the target devices both theoretically and experimentally. It is reported that there is an interfacial degradation reaction [as illustrated in Eq. (1) and (2)] between Ni^{3+} on the surface of NiO_x HTL and A-site cationic salt in perovskite, which will accelerate the reduction of $Ni^{\geq 3+}$ to $Ni^{\geq 2+}$ in NiO_x film and the degradation of perovskite, and generate interstitial iodine through deprotonating A-site cation and oxidizing iodide species, resulting in serious instability of device:[59,60]

$$HAPbI_3 \leftrightarrow PbI_2 + A_{(g)} + \frac{1}{2}I_{2(g)} + H^+ + e^- \quad (1)$$

$$Ni^{\geq 3+}O_x + e^- + H^+ \leftrightarrow Ni^{\geq 2+}O_xH \quad (2)$$

where HA^+ is the protonated A-site cation (such as $CH_3NH_3^+$ and $NH{=}CH{-}NH_3^+$), and A is the deprotonated A-site cation (CH_3NH_2 and $NH{=}CH{-}NH_2$).

DFT calculations have been used to investigate the effect of NO_3^- and $[BMIm]^+$ on reactions (1) and (2). The reaction energy of Equation (1) is the same, which comes from the decomposition of perovskite. The reaction energy of Equation (2) can be described as follows Equations (3) and (4):

$$\Delta E(NO_3^-) = E(Ni^{\geq 2+}O_xH{-}NO_3^-) - E(Ni^{\geq 3+}O_x{-}NO_3^-) - E(H^+ + e^-) \quad (3)$$

$$\Delta E((BMIm)^+) = E(Ni^{\geq 2+}O_xH{-}(BMIm)^+) - E(Ni^{\geq 3+}O_x{-}(BMIm)^+) - E(H^+ + e^-) \quad (4)$$

Among them, $E(Ni^{\geq 3+}O_x{-}NO_3^-)$, $E(Ni^{\geq 3+}O_x{-}(BMIm)^+)$, $E(Ni^{\geq 2+}O_xH{-}NO_3^-)$ and $E(Ni^{\geq 2+}O_xH{-}(BMIm)^+)$ represent the energy of NO_3^-, $[BMIm]^+$, NO_3^- and H, $[BMIm]^+$ and H adsorbed on the NiO surface, respectively. According to the theoretical calculation (Figure 4a), the reaction energy difference between Equation (3) and (4) is 0.43 eV, indicating that the energy of $[BMIm]^+$ adsorption in Equation (4) is lower than that of NO_3^- adsorption in formula (3). This result means that the $[BMIm]^+$ adsorption can effectively slow the progression of Equation (2), thereby delaying the oxidation-reduction reaction at the NiO/perovskite interface. Meanwhile, for NiO and NiO-IL, the number of electron transfer was 0.62 and 0.60 e (Figure 4b), respectively. From the results of the two-dimensional (2D) slices of charge density distribution (Figure 4c), the H–O interaction is formed between the NO_3^- impurity ions in control NiO and the adsorbed H^+ produced by perovskite decomposition [Eq. (1)], leading to stronger adsorption of H^+ on the control NiO, which prompts the redox reactions at the NiO/perovskite interface and accelerates the decomposition of perovskite layer. Based on the above results, the NiO_x-IL greatly reduces the adverse factors existing in control NiO_x (Figure 4d), thus effectively improving the stability of device.

We also verified the influence degree of NO_3^- and $[BMIm]^+$ adsorption on the interfacial reaction between NiO_x and perovskite through experiments. It can be seen from Equation (2) that H^+ in control NiO_x and NiO_x-IL all comes from the decomposition of perovskite materials in Equation (1), and the charge of exogenous ions could have a direct influence on the reaction in Equation (2). We used photographs and UV/Vis spectra to indentify the degree of reaction of NiO_x films treated by pure MAI perovskite precursor, MAI perovskite precursor containing NO_3^-, or $[BMIm]^+$ according to the work of McGehee et al.[59] The detailed methods are illustrated in Supplementary Notes. As illustrated in Figure 4e, the NiO_x surface was bleached after the pure MAI solution treatment; and the MAI solution containing NO_3^- bleached the NiO_x surface more obviously. On the contrary, the MAI solution containing $[BMIm]^+$ did not cause obvious change on NiO_x surface. The corresponding UV/Vis spectra also confirmed our observation (Figure 4f). From our analysis (Figure 4d), the negative charge of NO_3^- impurity ions could promote the reaction (2), thus accelerating the decomposition of MAI in the reaction (1); on the contrary, the introduction of $[BMIm]^+$ could

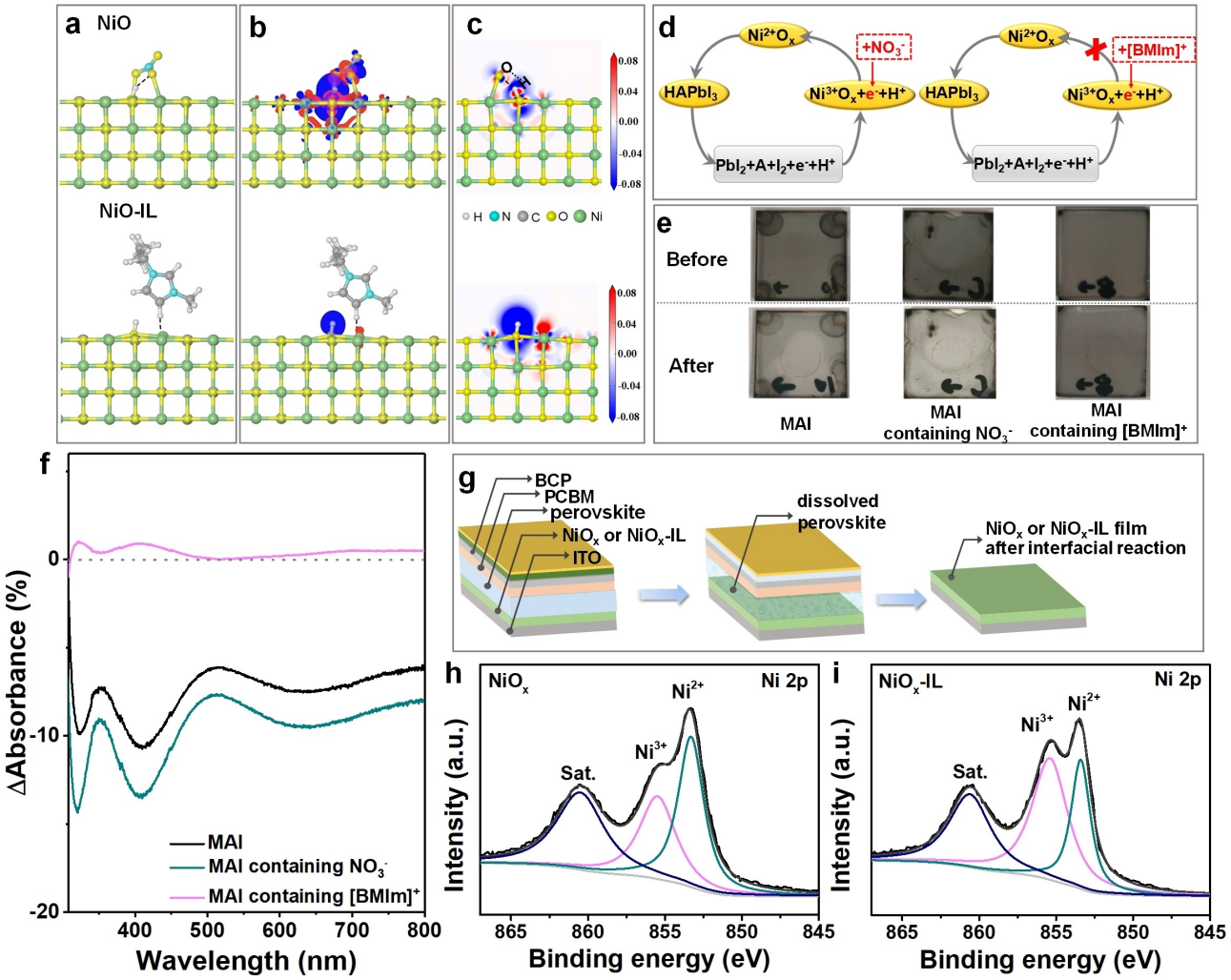

Figure 4. H atom adsorbs on the NiO (100) surface containing NO_3^- and $[BMIm]^+$: a) optimized geometry b) charge density difference (isovalue is 0.003 e bohr^{-3} for NO_3^- adsorption, and 0.08 e bohr^{-3} for $[BMIm]^+$ adsorption). c) the 2D slice of charge density difference. d) Schematic diagram of the influence of NO_3^- impurity ions and $[BMIm]^+$ additive on the redox reaction between the interface. e) Photographs of NiO_x films after treatment with a drop of pure MAI perovskite precursor, MAI precursor containing NO_3^-, or $[BMIm]^+$, respectively. f) Change in absorbance of NiO_x films treated with various solutions. g) Schematic diagram of method for testing the effect of oxidation-reduction reaction at the NiO_x/perovskite interface on the change of Ni^{3+} content in NiO_x and NiO_x-IL films; XPS spectra of Ni 2p in h) NiO_x and i) NiO_x-IL films after long-term operational stability measurements (one sun, ambient air, MPP tracking, 1000 h).

effectively inhibit the adsorption of NO_3^- in NiO_x and slow down the interfacial degradation reaction. The above results further indicate that the presence of $[BMIm]^+$ can effectively suppress the reaction between NiO_x and perovskite precursor materials, which plays a positive role in improving the stability of the device. Additionally, we investigated the changes of elements in MAI after the reaction between NiO_x film and MAI by XPS. As shown in Figure S21 and S22 in Supporting Information, compared with pristine NiO_x film, the XPS spectra of I 3d in NiO_x film treated with MAI solution shows lower intensity, and the MA^+ species are mostly transformed into MA. The results imply that Ni^{3+} defect sites exhibit Brønsted acid–base properties and deprotonate the MA^+, further confirming the above (1) and (2) reactions between the interfaces.

According to the redox reaction between the interface of NiO_x or NiO_x-IL HTL and perovskite layer, the amount of Ni^{3+} in HTL decreases and the amount of Ni^{2+} increases during the reaction process. Therefore, we used lift-off method (Figure 4g, the details are described in Supporting Information) to concretely study the content changes of Ni^{3+} and Ni^{2+} in NiO_x and NiO_x-IL buried films after the interfacial reaction for long-term actual operation (above operational stability measurements: one sun, ambient air, MPP tracking, 1000 h).[59,61] As shown in Figure 4h, it is calculated that the ratio of Ni^{3+}/Ni^{2+} in the control NiO_x film decreases from 1.35 to 0.77, while the Ni^{3+}/Ni^{2+} ratio of NiO_x-IL film decreases slightly from 1.92 to 1.71. The results clearly show that the NiO_x-IL HTL assisted by the $[BMIm]BF_4$ IL can effectively delay the redox reaction between the HTL/perovskite layer interface and reduce the

reduction of Ni^{3+} to Ni^{2+}, inhibit the decomposition of perovskite material, and ultimately improve the operational stability of device.

Conclusion

In this work, we innovatively synthesized NiO_x-IL assisted by $[BMIm]BF_4$ IL to obtain high quality HTL. On the one hand, experimental and theoretical results show that the $[BMIm]BF_4$ IL forms a strong hydrogen bond with nickel hydroxide, effectively hindering the existence of the impurity ligand NO_3^- in NiO_x HTL and improving the conductivity of the corresponding HTL; on the other hand, compared with the control NiO_x-containing impurity, the removal of NO_3^- ions can effectively slow down the redox reaction at the NiO_x/perovskite interface, thus improving the stability of the device. As a consequence, NiO_x-IL as HTL enabled the hysteresis-free device with an efficiency of up to 22.62 %. More importantly, the device based on NiO_x-IL showed a significant improvement in ambient air and remained 90 % of its initial PCE for 6000 h. Furthermore, remarkable operational stability was also realized in the modified encapsulated device which can retain 92 % of the initial efficiency after 1000 h at MPP tracking under one-sun irradiation. This strategy provides a new understanding for the interfacial reaction of PSCs and opens a new route for improving the performance of the HTL.

Acknowledgements

This research is supported by the National Natural Science Foundation of China (52172237, 52072228), the Shaanxi International Cooperational Project (2020KWZ-018), the Research Fund of the State Key Laboratory of Solidification Processing (NPU), China (Grant No. 2021-QZ-02), and the Fundamental Research Funds for the Central Universities (3102019JC005). We thank the members from the Analytical & Testing Center of Northwestern Polytechnical University for the help of XPS, UPS, AFM and SEM characterization.

Conflict of Interest

The authors declare no conflict of interest.

Data Availability Statement

Research data are not shared.

Keywords: Hole Transport Layer · Interfacial Redox Reaction · Nickel Oxide · Perovskite Solar Cells

[1] H. Zhu, Y. Ren, L. Pan, O. Ouellette, F. T. Eickemeyer, Y. Wu, X. Li, S. Wang, H. Liu, X. Dong, S. M. Zakeeruddin, Y. Liu, A. Hagfeldt, M. Grätzel, *J. Am. Chem. Soc.* **2021**, *143*, 3231–3237.
[2] Q. Zhou, J. Qiu, Y. Wang, M. Yu, J. Liu, X. Zhang, *ACS Energy Lett.* **2021**, *6*, 1596–1606.
[3] B. Chen, H. Chen, Y. Hou, J. Xu, S. Teale, K. Bertens, H. Chen, A. Proppe, Q. Zhou, D. Yu, K. Xu, M. Vafaie, Y. Liu, Y. Dong, E. H. Jung, C. Zheng, T. Zhu, Z. Ning, E. H. Sargent, *Adv. Mater.* **2021**, *33*, 2103394.
[4] X. Yin, Y. Guo, H. Xie, W. Que, L. B. Kong, *Sol. RRL* **2019**, *3*, 1900001.
[5] L. Xu, X. Chen, J. Jin, W. Liu, B. Dong, X. Bai, H. Song, P. Reiss, *Nano Energy* **2019**, *63*, 103860.
[6] F. Sadegh, S. Akin, M. Moghadam, R. Keshavarzi, V. Mirkhani, M. A. Ruiz-Preciado, E. Akman, H. Zhang, M. Amini, S. Tangestaninejad, I. Mohammadpoor-Baltork, M. Grätzel, A. Hagfeldt, W. Tress, *Adv. Funct. Mater.* **2021**, *31*, 2102237.
[7] I. S. Yang, M. R. Sohn, S. D. Sung, Y. J. Kim, Y. J. Yoo, J. Kim, W. I. Lee, *Nano Energy* **2017**, *32*, 414–421.
[8] S. Ye, W. Sun, Y. Li, W. Yan, H. Peng, Z. Bian, Z. Liu, C. Huang, *Nano Lett.* **2015**, *15*, 3723–3728.
[9] H. Zhang, J. Cheng, F. Lin, H. He, J. Mao, S. W. Kam, K.-Y. Alex, C. H. C. Wallace, *ACS Nano* **2016**, *10*, 1503–1511.
[10] X. Yin, P. Chen, M. Que, Y. Xing, W. Que, C. Niu, J. Shao, *ACS Nano* **2016**, *10*, 3630–3636.
[11] T. Wang, D. Ding, H. Zheng, X. Wang, J. Wang, H. Liu, W. Shen, *Sol. RRL* **2019**, *3*, 1900045.
[12] S. Sajid, A. M. Elseman, D. Wei, J. Ji, S. Dou, H. Huang, P. Cui, M. Li, *Nano Energy* **2019**, *55*, 470–476.
[13] W. Sun, S. Ye, H. Rao, Y. Li, Z. Liu, L. Xiao, Z. Chen, Z. Bian, C. Huang, *Nanoscale* **2016**, *8*, 15954–15960.
[14] W.-Y. Chen, L.-L. Deng, S.-M. Dai, X. Wang, C.-B. Tian, X.-X. Zhan, S.-Y. Xie, R.-B. Huang, L.-S. Zheng, *J. Mater. Chem. A* **2015**, *3*, 19353–19359.
[15] J. Wang, J. Li, Y. Zhou, C. Yu, Y. Hua, Y. Yu, R. Li, X. Lin, R. Chen, H. Wu, H. Xia, H. L. Wang, *J. Am. Chem. Soc.* **2021**, *143*, 7759–7768.
[16] H. Bao, M. Du, H. Wang, K. Wang, X. Zuo, F. Liu, L. Liu, D. Eder, A. Cherevan, S. Wang, L. Wan, S. Zhao, S. Liu, *Adv. Funct. Mater.* **2021**, *31*, 2102452.
[17] F. Cheng, R. He, S. Nie, C. Zhang, J. Yin, J. Li, N. Zheng, B. Wu, *J. Am. Chem. Soc.* **2021**, *143*, 5855–5866.
[18] S. Wang, B. Yang, J. Han, Z. He, T. Li, Q. Cao, J. Yang, J. Suo, X. Li, Z. Liu, S. Liu, C. Tang, A. Hagfeldt, *Energy Environ. Sci.* **2020**, *13*, 5068–5079.
[19] Q. Cao, J. Yang, T. Wang, Y. Li, X. Pu, J. Zhao, Y. Zhang, H. Zhou, X. Li, X. Li, *Energy Environ. Sci.* **2021**, *14*, 5406–5415.
[20] Q. Cao, Y. Li, H. Zhang, J. Yang, J. Han, T. Xu, S. Wang, Z. Wang, B. Gao, J. Zhao, X. Li, X. Ma, S. Zakeeruddin, W. Sha, X. Li, M. Grätzel, *Sci. Adv.* **2021**, *7*, eabg0633.
[21] W. Chen, Y. Zhou, G. Chen, Y. Wu, B. Tu, F. Z. Liu, L. Huang, A. M. C. Ng, A. B. Djurišić, Z. He, *Adv. Energy Mater.* **2019**, *9*, 1803872.
[22] X. Lian, J. Chen, S. Shan, G. Wu, H. Chen, *ACS Appl. Mater. Interfaces* **2020**, *12*, 46340–46347.
[23] K. C. Wang, J. Y. Jeng, P. S. Shen, Y. C. Chang, E. W. Diau, C. H. Tsai, T. Y. Chao, H. C. Hsu, P. Y. Lin, P. Chen, T. F. Guo, T. C. Wen, *Sci. Rep.* **2014**, *4*, 4756.
[24] S. Seo, I. J. Park, M. Kim, S. Lee, C. Bae, H. S. Jung, N. G. Park, J. Y. Kim, H. Shin, *Nanoscale* **2016**, *8*, 11403–11412.
[25] M. Jung, Y. C. Kim, N. J. Jeon, W. Yang, J. Seo, J. H. Noh, S. Seok, *ChemSusChem* **2016**, *9*, 2592–2596.
[26] J. H. Park, J. Seo, S. Park, S. S. Shin, Y. C. Kim, N. J. Jeon, H. W. Shin, T. K. Ahn, J. H. Noh, S. C. Yoon, C. S. Hwang, S. I. Seok, *Adv. Mater.* **2015**, *27*, 4013–4019.

[27] J.-J. Zhao, X. Su, Z. Mi, Y. Zhang, Y.-J. Hu, H.-J. Guo, Y.-N. Jiao, Y.-X. Zhang, Y. Shi, W.-Z. Hao, J.-W. Wu, Y. Wang, C.-F. Gao, G.-Z. Cao, *Rare Met.* **2022**, *41*, 96–105.
[28] S. Zhumagali, F. H. Isikgor, P. Maity, J. Yin, E. Ugur, M. De Bastiani, A. S. Subbiah, A. J. Mirabelli, R. Azmi, G. T. Harrison, J. Troughton, E. Aydin, J. Liu, T. Allen, A. U. Rehman, D. Baran, O. F. Mohammed, S. Wolf, *Adv. Energy Mater.* **2021**, *11*, 2101662.
[29] W. Chen, Y. Zhou, L. Wang, Y. Wu, B. Tu, B. Yu, F. Liu, H. W. Tam, G. Wang, A. B. Djurisic, L. Huang, Z. He, *Adv. Mater.* **2018**, *30*, 1800515.
[30] P. Ru, E. Bi, Y. Zhang, Y. Wang, W. Kong, Y. Sha, W. Tang, P. Zhang, Y. Wu, W. Chen, X. Yang, H. Chen, L. Han, *Adv. Energy Mater.* **2020**, *10*, 1903487.
[31] J. W. Jung, C. C. Chueh, A. K. Jen, *Adv. Mater.* **2015**, *27*, 7874–7880.
[32] J. Ciro, D. Ramirez, M. A. Mejia Escobar, J. F. Montoya, S. Mesa, R. Betancur, F. Jaramillo, *ACS Appl. Mater. Interfaces* **2017**, *9*, 12348–12354.
[33] R. Li, P. Wang, B. Chen, X. Cui, Y. Ding, Y. Li, D. Zhang, Y. Zhao, X. Zhang, *ACS Energy Lett.* **2020**, *5*, 79–86.
[34] T. Mahmoudi, Y. Wang, Y.-B. Hahn, *Nano Energy* **2021**, *79*, 105452.
[35] J. He, E. Bi, W. Tang, Y. Wang, Z. Zhou, X. Yang, H. Chen, L. Han, *Sol. RRL* **2018**, *2*, 1800004.
[36] W. Chen, Y. Wu, Y. Yue, J. Liu, W. Zhang, X. Yang, H. Chen, E. Bi, I. Ashraful, M. Grätzel, *Science* **2015**, *350*, 944–948.
[37] Q. Wang, C.-C. Chueh, T. Zhao, J. Cheng, M. Eslamian, M. Eslamian, W. C. H. Choy, A. K.-Y. Jen, *ChemSusChem* **2017**, *10*, 3794–3803.
[38] Z. Li, B. H. Jo, S. J. Hwang, T. H. Kim, S. Somasundaram, E. Kamaraj, J. Bang, T. K. Ahn, S. Park, H. J. Park, *Adv. Sci.* **2019**, *6*, 1802163.
[39] L. Wang, L. Chang, B. Zhao, Z. Yuan, G. Shao, W. Zheng, *Inorg. Chem.* **2008**, *47*, 1443–1452.
[40] T. Gao, B. P. Jelle, *J. Phys. Chem. C* **2013**, *117*, 17294–17302.
[41] M. G. Freire, C. M. S. S. Neves, I. M. Marrucho, J. A. P. Coutinho, A. M. Fernandes, *J. Phys. Chem. A* **2010**, *114*, 3744–3749.
[42] D. A. Shirley, P. W. Alley, *J. Am. Chem. Soc.* **1957**, *79*, 4922–4927.
[43] D. S. Hall, D. J. Lockwood, S. Poirier, C. Bock, B. R. MacDougall, *J. Phys. Chem. A* **2012**, *116*, 6771–6784.
[44] D. S. Hall, D. J. Lockwood, S. Poirier, C. Bock, B. R. MacDougall, *ACS Appl. Mater. Interfaces* **2014**, *6*, 3141–3149.
[45] C. Y. Xu, W. Hu, G. Wang, L. Niu, A. M. Elseman, L. Liao, Y. Yao, G. Xu, L. Luo, D. Liu, G. Zhou, P. Li, Q. Song, *ACS Nano* **2020**, *14*, 196–203.
[46] S. Uhlenbrock, C. Scharfschwerdt, M. Neumann, G. Illing, H.-J. Freund, *J. Phys. Condens. Matter* **1992**, *4*, 7973–7978.
[47] B. Sasi, K. G. Gopchandran, *Nanotechnology* **2007**, *18*, 115613.
[48] L. Yao, S. Zhang, R. Wang, W. Li, F. Shen, B. Yang, Y. Ma, *Angew. Chem. Int. Ed.* **2014**, *53*, 2119–2123; *Angew. Chem.* **2014**, *126*, 2151–2155.
[49] J. R. Manders, S.-W. Tsang, M. J. Hartel, T.-H. Lai, S. Chen, C. M. Amb, J. R. Reynolds, *Adv. Funct. Mater.* **2013**, *23*, 2993–3001.
[50] N. Pant, M. Yanagida, Y. Shirai, K. Miyano, *Appl. Phys. Express* **2020**, *13*, 025505.
[51] H. Lee, W. Yang, J. Tan, Y. Oh, J. Park, J. Moon, *ACS Energy Lett.* **2019**, *4*, 995–1003.
[52] J. He, Y. Xiang, F. Zhang, J. Lian, R. Hu, P. Zeng, J. Song, J. Qu, *Nano Energy* **2018**, *45*, 471–479.
[53] W. Chen, G. Pang, Y. Zhou, Y. Sun, F.-Z. Liu, R. Chen, S. Chen, A. B. Djurišić, Z. He, *J. Mater. Chem. A* **2020**, *8*, 1865–1874.
[54] W. Chen, Y. Wu, J. Fan, A. B. Djurišić, F. Liu, H. W. Tam, A. Ng, C. Surya, W. K. Chan, D. Wang, Z.-B. He, *Adv. Energy Mater.* **2018**, *8*, 1703519.
[55] S. Apergi, G. Brocks, S. Tao, *Phys. Rev. Mater.* **2020**, *4*, 085403.
[56] T. Kirchartz, J. A. Márquez, M. Stolterfoht, T. Unold, *Adv. Energy Mater.* **2020**, *10*, 1904134.
[57] C. M. Wolff, P. Caprioglio, M. Stolterfoht, D. Neher, *Adv. Mater.* **2019**, *31*, 1902762.
[58] M. Stolterfoht, P. Caprioglio, C. M. Wolff, J. A. Márquez, J. Nordmann, S. Zhang, D. Rothhardt, U. Hormann, Y. Amir, A. Redinger, L. Kegelmann, F. Zu, S. Albrecht, N. Koch, T. Kirchartz, M. Saliba, T. Unold, D. Neher, *Energy Environ. Sci.* **2019**, *12*, 2778.
[59] C. C. Boyd, R. C. Shallcross, T. Moot, R. Kerner, L. Bertoluzzi, A. Onno, S. Kavadiya, C. Chosy, E. J. Wolf, J. Werner, J. A. Raiford, C. de Paula, A. F. Palmstrom, Z. J. Yu, J. J. Berry, S. F. Bent, Z. C. Holman, J. M. Luther, E. L. Ratcliff, N. R. Armstrong, M. D. McGehee, *Joule* **2020**, *4*, 1759–1775.
[60] J. Zhang, J. Long, Z. Huang, J. Yang, X. Li, R. Dai, W. Sheng, L. Tan, Y. Chen, *Chem. Eng. J.* **2021**, *426*, 131357.
[61] I. Levine, A. Al-Ashouri, A. Musiienko, H. Hempel, A. Magomedov, A. Drevilkauskaite, V. Getautis, D. Menzel, K. Hinrichs, T. Unold, S. Albrecht, T. Dittrich, *Joule* **2021**, *5*, 2915–2933.

Manuscript received: December 4, 2021
Accepted manuscript online: February 17, 2022
Version of record online: March 4, 2022